Fermionic Quantum Circuits Reproduce Experimental Two-dimensional Many-body Localization Transition Point

Joey Li,¹ Amos Chan,² and Thorsten B. Wahl³

¹Department of Physics and Institute for Condensed Matter Theory, University of Illinois at Urbana-Champaign, Urbana, Illinois 61801, USA. ²Princeton Center for Theoretical Science, Princeton University, Princeton New Jersey 08544, USA ³DAMTP, University of Cambridge, Wilberforce Road, Cambridge, CB3 0WA, United Kingdom. (Dated: September 10, 2021)

While many-body localization (MBL) is a well-established phenomenon in one-dimension, the fate of higher-dimensional strongly disordered systems in the infinite-time limit is a topic of current debate. The latest experiments as well as several recent numerical studies indicate that such systems behave many-body localized – at least on practically relevant time scales. However, thus far, theoretical approaches have been unable to quantitatively reproduce experimentally measured MBL features, an important requirement to demonstrate their validity. Here, we develop a formalism to apply fermionic quantum circuits combined with automatic differentiation to simulate two-dimensional MBL systems realized in optical lattice experiments with fermions. Using entanglement-based features, we obtain a phase transition point in excellent agreement with the experimentally measured value. We argue that our approach best captures the underlying charge-density-wave experiments and calculate other quantities which can be compared to future experiments, such as the mean localization lengths.

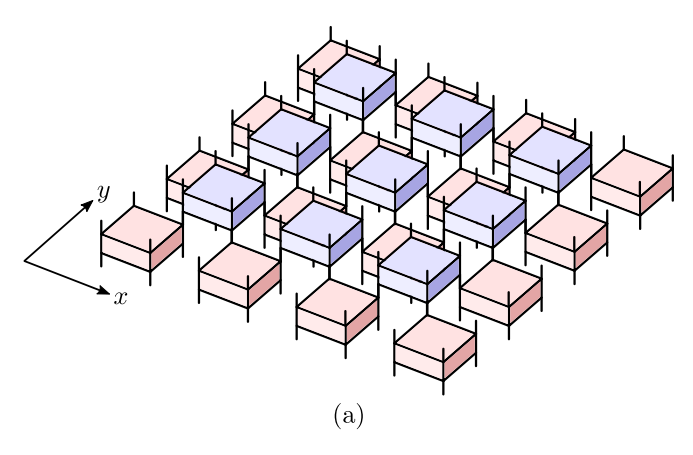
Introduction. — An important requirement for the laws of thermodynamics to be meaningful is that closed systems act as their own heat baths. For quantum many-body systems, this requirement is expressed in the eigenstate thermalization hypothesis [1, 2] (ETH). However, with the discovery of many-body localization [3–5] (MBL), it became apparent that not only fine-tuned systems are able to evade the ETH [6], but that there exists an entire phase of matter that lacks thermalization. For one-dimensional strongly disordered quantum systems, the existence of MBL is well-established through various numerical studies [7–10], experimental observations [11–15] and a recent rigorous proof using only very mild assumptions [16].

In two dimensions, MBL would allow for topologicallyprotected quantum computation away from low temperatures [18–21], a promising feature as we enter the era of noisy intermediate-scale quantum computing [22]. However, whether MBL exists beyond one dimension is still an important open question: Experimental observations are supportive of higher-dimensional MBL [23-25], and several theoretical studies are also in favor of this scenario [26–36], while others plead against it [37–39]. A possible explanation of these divergent results is that strongly disordered quantum systems in higher dimensions eventually thermalize but on extremely long time scales [38, 40]. As a result, it is likely that such systems can be viewed as many-body localized on all experimentally relevant time scales. Hence, the practically most relevant task is the description of the phenomenon of higher-dimensional MBL on those time scales.

In this work, we use shallow fermionic two-dimensional quantum circuits to simulate the MBL-to-thermal transition observed in optical lattice experiments with fermions

subject to a quasi-periodic potential [24]. We obtain a phase transition point in excellent agreement with the one measured experimentally and argue that this is due to the corresponding charge-density-wave initializations being well captured by shallow quantum circuit simulations.

Quantum circuits have proven to be a powerful tool, both for the numerical simulation of MBL [27, 41, 42] and the analytical classification of symmetry-protected topological MBL phases [43–45]. As opposed to other approaches, quantum circuits approximate the full set of eigenstates in the MBL regime and give access to all their local observables. In one dimension, this feature allows to reproduce the MBL-to-thermal transition point [42] found in exact diagonalization studies [46], even for very simple quantum circuit architectures. However, while two-dimensional quantum circuit simulations display striking features of an MBL phase in the strongly disordered regime [27], they significantly overestimate the phase transition point found in bosonic optical lattice experiments [23]. While these were initialized with one half of the optical trap filled, the fermionic optical lattice experiments of Ref. [24] were initialized with charge-density-waves. This gives quantum circuit simulations two important advantages over the bosonic experiments: (i) The numerical simulations do not require a truncation of the on-site Hilbert space dimension. (ii) Charge-density-waves require only few hops of the atoms to reach thermal equilibrium, a process more amenable to a description by shallow quantum circuits. We note that fermionic quantum circuit simulations do not suffer from the sign problem plaguing Monte Carlo approaches. We calculate the transition point as a function of the filling fraction, reproducing the experimental result of Ref. [24]



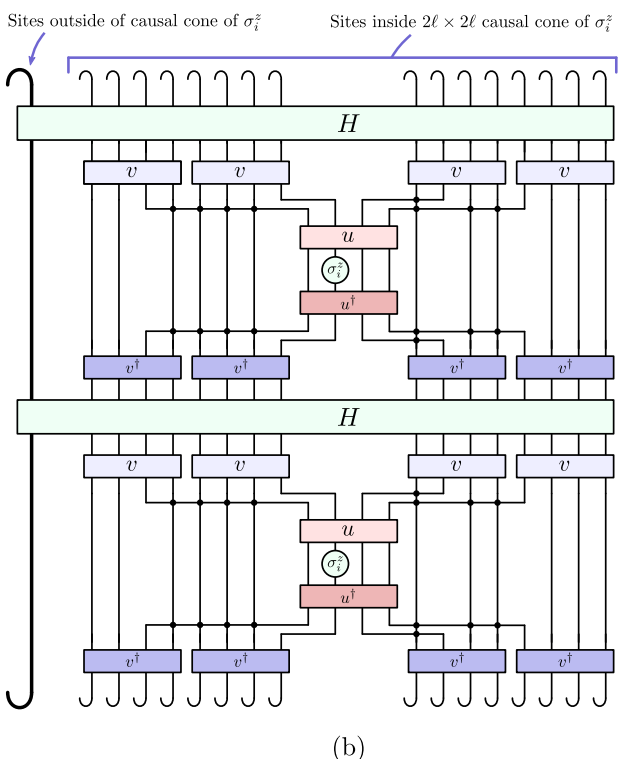


FIG. 1. (a) The tensor network \tilde{U} composed of two layers of unitary gates (blue and red) arranged in a brick-wall geometry. (b) \tilde{U} is obtained by minimizing $-\operatorname{Tr}(H\tilde{\tau}^z_{i,\mu}H\tilde{\tau}^z_{i,\mu})$ (illustrated), which depends only on a (roughly) $2\ell \times 2\ell$ causal cone of $\sigma^z_{i,\mu}$. The black dots correspond to fermionic swap gates, and the indices outside of the causal cone are denoted collectively as a thick line. See [17] for details.

at half filling. We also compute the average localization length as a function of disorder strength, which can be easily compared to future domain wall experiments [23].

Formalism. — In one dimension, MBL systems have been shown to possess a complete set of local integrals of motion [47–55] (LIOMs), also known as l-bits. For a spin-1/2 chain, they are typically denoted as τ_i^z and by definition commute with the MBL Hamiltonian H_{1D} and with each other, $[H_{1D}, \tau_i^z] = [\tau_i^z, \tau_i^z] = 0$. The LIOMs

are related via a local unitary [56] U (which also diagonalizes the Hamiltonian) to the on-site spin-z Pauli operators, $\tau_i^z = U \sigma_i^z U^\dagger$. As a result, τ_i^z is exponentially localized around site i, where the corresponding characteristic decay length is known as the localization length ξ_L . The Hamiltonian can be expressed in terms of LIOMs, $H_{1D} = c + \sum_i c_i \tau_i^z + \sum_{i,j} c_{ij} \tau_i^z \tau_j^z + \sum_{i,j,k} c_{ijk} \tau_i^z \tau_j^z \tau_k^z + \ldots$, where $|c_{ijk...}|$ decays exponentially with the maximum distance between the indexed sites.

In two dimensions, any set of local quantities $\{\tau_i^z\}$ may not exactly commute with the Hamiltonian; however, the inverse of the commutator in operator norm $||[H_{2D}, \tau_i^z]||_{\text{op}}$ serves as a lower bound on relaxation times [40]. Hence, systems with a very small commutator behave many-body localized on very long time scales [38, 40], giving rise to the experimental observation of two-dimensional MBL. Setting aside the question whether MBL persists in the infinite-time limit, here we use fermionic quantum circuits \tilde{U} to describe the MBL-to-thermal transition found in optical lattice experiments with fermions [24]. To that end, we construct a set of approximate LIOMs $\tilde{\tau}_i^z = \tilde{U}\sigma_i^z\tilde{U}^{\dagger}$ [27]. We optimize the unitaries constituting the quantum circuit Uby minimizing the commutator with the Hamiltonian in fermionic trace norm $\sum_{i} ||[H, \tilde{\tau}_{i}^{z}]||_{\mathrm{tr}}^{2}$, which thus enables us to describe MBL-like behavior on experimentally relevant time scales. The likely transience of MBL in two dimensions also implies that the transition seen in experiments is actually a (relatively abrupt [38]) crossover between a quickly thermalizing regime and a regime where thermalization takes place on non-accessible time scales. It is currently unclear whether the arguments in favor of metastable MBL also apply to quasi-periodic systems [37, 57]. We use the semantics of a transition throughout this manuscript, keeping these aspects in mind.

Model and numerical approach. — We study the model Hamiltonian underlying the fermionic optical lattice experiments of Ref. [24]. The system consists of spin-1/2 fermions on a two-dimensional $N \times N$ square lattice governed by the Fermi-Hubbard Hamiltonian with a quasi-periodic potential,

$$H = -J \sum_{\langle i,j \rangle} \sum_{\mu=\uparrow,\downarrow} (c_{i,\mu}^{\dagger} c_{j,\mu} + c_{j,\mu}^{\dagger} c_{i,\mu}) + V \sum_{i} n_{i,\uparrow} n_{i,\downarrow}$$
$$+ \Delta \sum_{i} \left[\cos(2\pi \beta_{x} x) + \cos(2\pi \beta_{y} y) \right] (n_{i,\uparrow} + n_{i,\downarrow}), \quad (1)$$

where the lattice sites are labeled by i=(x,y). $c_{i,\mu}^{\dagger}$, $c_{i,\mu}$, $c_{i,\mu}$ are fermionic creation and annihilation operators with spin-z component $\mu=\uparrow,\downarrow$, and $n_{i,\mu}=c_{i,\mu}^{\dagger}c_{i,\mu}$ is the particle number operator. Using the experimental model parameters, we set $\beta_x=0.721$ and $\beta_y=0.693$, and the on-site interaction strength to V=5J. Δ is the disorder strength; experimentally the MBL phase was observed

above the critical disorder strength $\Delta_c^{\text{exp}} = 9 \pm 0.5 J$.

In our computational approach, we consider multiple disorder realizations of a 10×10 system with periodic boundary conditions to emulate the properties of the experimental system in the center of the optical trap. To produce different disorder realizations, we shift the quasiperiodic potential by a random amount, i.e. we use the potential $\Delta[\cos(2\pi(\beta_x x + \delta x)) + \cos(2\pi(\beta_y y + \delta y))]$ with $\delta x, \delta y \in [0,1)$ drawn from a uniform distribution, where we keep the same choices for different Δ . We use a twolayer quantum circuit U with the same architecture as in Ref. [27], cf. Fig. 1a. The constituting unitaries generally act on patches of $\ell \times \ell$ sites. Here, we choose $\ell = 2$ and restrict the unitaries to be real and to preserve particle number (as the overall Hamiltonian does), which also ensures they have even parity. In order to optimize them, we fermionize the algorithm described in Ref. [27], which requires minimizing the cost function

$$f(\tilde{U}) = \frac{1}{N^2 4^{N^2}} \sum_{i} \sum_{\mu=\uparrow,\downarrow} \left[\text{Tr}(H^2) - \text{Tr}(H\tilde{\tau}_{i,\mu}^z H \tilde{\tau}_{i,\mu}^z) \right],$$
(2)

whose tensor network representation is shown in Fig. 1b. Here, we have to account for the fact that the on-site Hilbert space dimension of the model is 4, i.e., there are two approximate LIOMs per site i, $\tilde{\tau}^z_{i,\mu}(\tilde{U}) = \tilde{U}\sigma^z_{i,\mu}\tilde{U}^\dagger$, where $\sigma^z_{i,\uparrow}$ acts on site i as $\sigma^z \otimes \mathbb{1}$ and $\sigma^z_{i,\downarrow}$ as $\mathbb{1} \otimes \sigma^z$. Expression (2) can be decomposed into a sum of local parts whose complexity is independent of the system size, allowing for the efficient optimization of the constituting unitaries using automatic differentiation [17].

Results. — We determined the location of the MBLto-thermal transition of this model by computing the on-site entanglement entropy S_i averaged over approximate eigenstates as a function of disorder strength Δ . Even though the Fock space dimension grows exponentially with the system size, this can be done in an efficient fashion using the approach outlined in [17, 27]. The standard deviation $\sigma_{S,i}$ of the averaged entanglement entropy with respect to disorder realizations peaks at the transition point [10]. To reduce statistical fluctuations, we average $\sigma_{S,i}$ over site positions i [27, 42], resulting in the behavior shown in Fig. 2. We observe a maximum at $\Delta_c \approx 9.1J$. This value corresponds to an average over 1,000 randomly chosen approximate eigenstates per disorder realization and all sites i. The filling fraction ν of almost all of these eigenstates is near its mean value of 1. However, the charge-density-wave evolutions of Ref. [24] only involved eigenstates with filling fraction $\nu = 0.5$ (as the particle number is a conserved quantity). Since lower filling fractions are associated with lower energies and the transition point depends on the energies of the involved eigenstates [27, 33, 46], our results need to be specified for filling fraction $\nu = 0.5$ in order to allow for an appropriate comparison with the experimental result. To

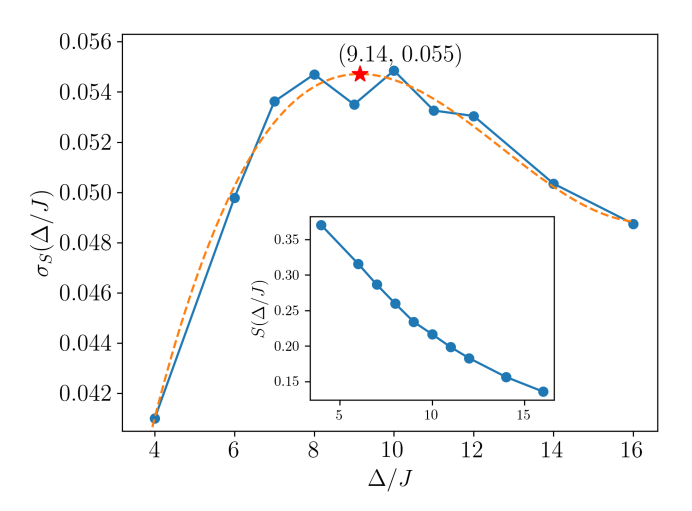


FIG. 2. Standard deviation, over 10 disorder realizations, of the entanglement entropy (averaged over 1,000 approximate eigenstates) as a function of Δ/J , averaged over sites. The dashed line is a third order polynomial fit. Inset: Entanglement entropy (averaged over sites, eigenstates, and disorder realizations) as a function of Δ/J .

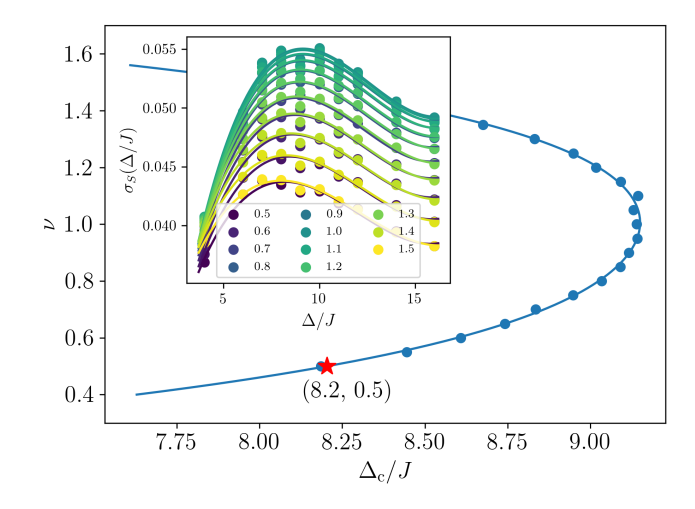


FIG. 3. Filling fraction-dependent phase diagram using a fourth order polynomial fit. The transition points were obtained from the maxima of the filling fraction-resolved entanglement entropy fluctuations (see inset).

that end, we carried out the above analysis by resolving the maximum of the site-averaged standard deviation of the entanglement entropy for different fillings. We show the filling fraction-resolved transition point $\Delta_c(\nu)$ in Fig. 3. The result at half filling, $\Delta_c(0.5)=8.2J$, is in excellent agreement with the experimental value of $\Delta_c^{\rm exp}=9\pm0.5J$ [24]. Combined with the calculation of the mobility edge in Ref. [27], this result demonstrates the tremendous potential of quantum circuit simulations to describe the phenomenon of two-dimensional many-

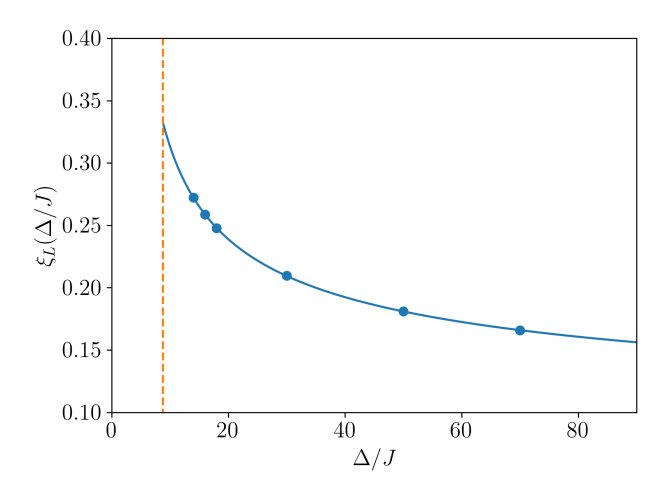


FIG. 4. Localization length ξ_L (in units of lattice spacing) as a function of Δ/J with a $1/\ln(\Delta/J)$ fit shown. The dashed line indicates the transition between the MBL and the thermal regime.

body localization on experimental time scales.

We also calculated the average localization length ξ_L as a function of disorder strength as a quantity which can be compared to future domain-wall experiments with fermions [23]. To that end, we adapted the weight function $w_i(\mathcal{O})$ introduced in Ref. [55] measuring the weight of a Hermitian operator \mathcal{O} on site i to fermionic spin-1/2 systems,

$$w_{i}(\mathcal{O}) = \sum_{\beta,\gamma}' \operatorname{Tr} \left[\left(\mathcal{O} - \hat{\sigma}_{i,\uparrow}^{\beta} \hat{\sigma}_{i,\downarrow}^{\gamma} \mathcal{O} \hat{\sigma}_{i,\downarrow}^{\gamma} \hat{\sigma}_{i,\uparrow}^{\beta} \right)^{2} \right], \quad (3)$$

where $\hat{\sigma}_{i,\mu}^x \equiv c_{i,\mu} + c_{i,\mu}^{\dagger}$, $\hat{\sigma}_{i,\mu}^y \equiv -ic_{i,\mu} + ic_{i,\mu}^{\dagger}$, $\hat{\sigma}_{i,\mu}^z \equiv 1 - 2c_{i,\mu}^{\dagger}c_{i,\mu}$, and $\hat{\sigma}_{i,\mu}^0 = 1$. The \sum' sum is defined over $\beta, \gamma \in \{0, x, y, z\}$, but omitting the term $\beta = \gamma = 0$. $w_i(\tilde{\tau}_{j,\mu}^z)$ can be calculated efficiently [17]. Within the causal cone of $\tilde{\tau}_{j,\mu}^z$ it decays exponentially with the distance between sites i and j. The corresponding decay length averaged over all sites i, j and disorder realisations yields ξ_L for a given disorder strength Δ . This is plotted in Fig. 4 and displays a $\xi_L(\Delta) \propto 1/\ln(\Delta/J)$ behavior for large Δ .

Discussion. — We now provide an argument why our approach reproduces the phase transition point found in charge-density-wave experiments with fermions, while the transition point computed in Ref. [27] is significantly higher than the one determined in "half-moon" experiments with bosons [23]: Strictly speaking, the transition point we find is not that of the original Hamiltonian H but of an auxiliary Hamiltonian \tilde{H} defined by the approximate LIOMs $\tilde{\tau}_i^z$, $\tilde{H} = \tilde{c} + \sum_i \tilde{c}_i \tilde{\tau}_i^z + \sum_{i,j} \tilde{c}_{ij} \tilde{\tau}_i^z \tilde{\tau}_j^z + \ldots$ (we suppress the $\mu = \uparrow, \downarrow$ indices here). The condition $\tilde{H} \approx H$ can be obtained by setting $\tilde{c}_{ijk...} := \frac{1}{4^{N^2}} \operatorname{Tr} \left(H \tilde{\tau}_i^z \tilde{\tau}_j^z \tilde{\tau}_k^z \ldots \right)$. Using the fact that $\tilde{\tau}_i^z = \tilde{U} \sigma_i^z \tilde{U}^\dagger$

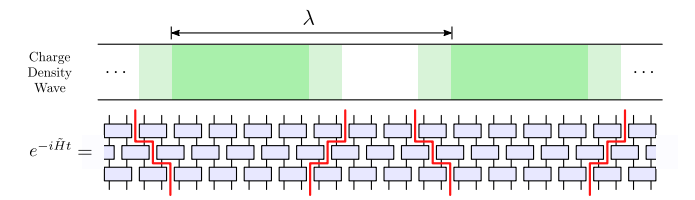


FIG. 5. Evolution of a charge-density-wave (top) of wavelength λ by $e^{-i\tilde{H}t}$ (bottom), which can be written as a one-dimensional 6-layer quantum circuit if it is projected on the x-axis. For simplicity, we only show 3 layers and $\ell=2$ with causal cones indicated by red lines. The propagated charge-density-wave (top) has regions of high charge density (green) and zero charge density (white). In general, the quantum circuit is able to propagate by $\mathcal{O}(\ell)$ columns (shown in light green).

and $H = \sum_m h_m$ (with two-site terms h_m), we obtain $\tilde{c}_{ijk...} = \frac{1}{4^{N^2}} \sum_m \text{Tr}(\tilde{U}^{\dagger} h_m \tilde{U} \sigma_i^z \sigma_j^z \sigma_k^z ...) \neq 0$ only if the sites i, j, k, ... all lie in one causal cone defined by any $U^{\dagger}h_mU$, whose maximum length is $L=3\ell$ (corresponding to a width of 2ℓ). Therefore, the time-evolution operator corresponding to the auxiliary Hamiltonian takes the $\text{form } e^{-i\tilde{H}\tilde{t}} \ = \ \tilde{U}e^{-i\tilde{c}t}\prod_{i}e^{-i\tilde{c}_{i}\sigma_{i}^{z}t}\prod_{i,j}e^{-i\tilde{c}_{ij}\sigma_{i}^{z}\sigma_{j}^{z}t}\ldots \tilde{U}^{\dagger},$ where we only keep factors $e^{-i\tilde{c}_{ijk...}\sigma_i^z\sigma_j^z\sigma_k^z...t}$ acting on plaquettes of at most $3\ell \times 2\ell$ sites. The product of these phase factors can be written as a two-layer quantum circuit U_{1D} with unitaries acting on $2L \times N$ sites [45] (i.e., it is a shallow quantum circuit only along the x-axis). Hence, $e^{-i\tilde{H}t} = \tilde{U}\tilde{U}_{1D}\tilde{U}^{\dagger}$ viewed along the x-axis is a six-layer quantum circuit, which can propagate particles at most across a distance of $d = 2L + 2\ell = 8\ell$ sites, cf. Fig. 5. However, as the unitaries of the numerically optimized quantum circuits are in general close to identities and the coefficients $\tilde{c}_{ijk...}$ exponentially suppressed with the maximum distance between the sites i, j, k, \ldots the Hamiltonian \hat{H} is expected to allow for equilibration over much less than $d=8\ell$ columns. Hence, $\ell=2$ simulations come much closer to the transition point obtained in charge-density-wave experiments [24] than with halfmoon initializations [23], which is why Ref. [27] overestimates the transition point: The "true" MBL-to-thermal transition point is upper bounded by the lowest disorder strength for which we find a non-thermalizing initialization, which is expected to be the half-moon configuration [23, 25]. However, due to the exponential decay of the coefficients $c_{ijk...}$, corresponding relaxation times can become extremely long, and it is not clear whether in the half-moon experiments observation times were sufficiently long to allow for these relaxation effects [24].

Conclusions. — We used a fermionic quantum circuit approach to simulate the two-dimensional MBL phase observed in optical lattice experiments with fermions. A careful analysis of the entanglement features for different filling fractions yielded an MBL-to-thermal transition

point in excellent agreement with the experimental result. Our obtained phase transition point as a function of filling fraction can be compared to future charge-densitywave experiments with occupied columns away from one fermion per site. We also calculated the average localization length as a function of disorder strength, another quantity which can be compared to future experiments. Finally, we provided an argument why quantum circuits built of unitaries acting on patches of 2×2 sites best capture the phase transition point found with chargedensity-wave initializations, explaining the discrepancy between the phase transition points found in Refs. [23] and [27]. A promising direction for future research is to increase ℓ and to analyze if the resulting phase transition points come closer to the result of half-moon experiments. Larger unit cells might also make it possible to test if regions of anomalously small disorder delocalize their environments, leading to the eventual breakdown of MBL in two dimensions [37, 58].

Acknowledgments. — We are grateful to David Huse, Rahul Nandkishore, and Steven Simon for useful discussions. TBW acknowledges support through the ERC Starting Grant No. 678795 TopInSy. AC is supported by fellowships from the Croucher Foundation and the PCTS at Princeton University.

- [1] J. M. Deutsch, Phys. Rev. A 43, 2046 (1991).
- [2] M. Srednicki, Phys. Rev. E 50, 888 (1994).
- [3] L. Fleishman and P. W. Anderson, Phys. Rev. B 21, 2366 (1980).
- [4] I. V. Gornyi, A. D. Mirlin, and D. G. Polyakov, Phys. Rev. Lett. 95, 206603 (2005).
- [5] I. L. Aleiner, B. L. Altshuler, and G. V. Shlyapnikov, Nat. Phys. 6, 900 (2010).
- [6] P. Anderson, Phys. Rev. 109, 1492 (1958).
- [7] M. Žnidarič, T. Prosen, and P. Prelovšek, Phys. Rev. B 77, 064426 (2008).
- [8] A. Pal and D. A. Huse, Phys. Rev. B 82, 174411 (2010).
- [9] J. H. Bardarson, F. Pollmann, and J. E. Moore, Phys. Rev. Lett. 109, 017202 (2012).
- [10] J. A. Kjäll, J. H. Bardarson, and F. Pollmann, Phys. Rev. Lett. 113, 107204 (2014).
- [11] M. Schreiber, S. S. Hodgman, P. Bordia, H. P. Lüschen, M. H. Fischer, R. Vosk, E. Altman, U. Schneider, and I. Bloch, Science 349, 842 (2015).
- [12] A. Lukin, M. Rispoli, R. Schittko, M. E. Tai, A. M. Kaufman, S. Choi, V. Khemani, J. Léonard, and M. Greiner, Science 364, 256 (2019).
- [13] J. Smith, A. Lee, P. Richerme, B. Neyenhuis, P. W. Hess, P. Hauke, M. Heyl, D. A. Huse, and C. Monroe, Nat. Phys. 12, 907 (2016).
- [14] P. Roushan et al., Science 358, 1175 (2017).
- [15] S. Choi, J. Choi, R. Landig, G. Kucsko, H. Zhou, J. Isoya, F. Jelezko, S. Onoda, H. Sumiya, V. Khemani, C. von Keyserlingk, N. Y. Yao, E. Demler, and M. D. Lukin, Nature 543, 221 (2017).

- [16] J. Z. Imbrie, J. Stat. Phys. 163, 998 (2016).
- [17] See supplementary material at [url] for diagrammatical approach to fermionic tensor network, evaluation of the local cost function and quantum circuit \tilde{U} , calculations of the entanglement entropy and localization lengths..
- [18] B. Bauer and C. Nayak, J. Stat. Mech., P09005 (2013).
- [19] D. A. Huse, R. Nandkishore, V. Oganesyan, A. Pal, and S. L. Sondhi, Phys. Rev. B 88, 014206 (2013).
- [20] Y. Bahri, R. Vosk, E. Altman, and A. Vishwanath, Nat. Comm. 6, 7341 (2015).
- [21] T. B. Wahl and B. Béri, Phys. Rev. Res. 2, 033099 (2020).
- [22] F. Arute, K. Arya, R. Babbush, D. Bacon, J. C. Bardin, et al., Nature (London) 574, 505 (2019).
- [23] J.-y. Choi, S. Hild, J. Zeiher, P. Schauß, A. Rubio-Abadal, T. Yefsah, V. Khemani, D. A. Huse, I. Bloch, and C. Gross, Science 352, 1547 (2016).
- [24] P. Bordia, H. Lüschen, S. Scherg, S. Gopalakrishnan, M. Knap, U. Schneider, and I. Bloch, Phys. Rev. X 7, 041047 (2017).
- [25] A. Rubio-Abadal, J.-y. Choi, J. Zeiher, S. Hollerith, J. Rui, I. Bloch, and C. Gross, Phys. Rev. X 9, 041014 (2019).
- [26] S. J. Thomson and M. Schiró, Phys. Rev. B 97, 060201(R) (2018).
- [27] T. B. Wahl, A. Pal, and S. H. Simon, Nat. Phys. 15, 164 (2019).
- [28] D. M. Kennes, arXiv:1811.04126.
- [29] H. Théveniaut, Z. Lan, G. Meyer, and F. Alet, Phys. Rev. Res. 2, 033154 (2020).
- [30] G. De Tomasi, F. Pollmann, and M. Heyl, Phys. Rev. B 99, 241114(R) (2019).
- [31] A. Kshetrimayum, M. Goihl, and J. Eisert, Phys. Rev. B 102, 235132 (2020).
- [32] E. Chertkov, B. Villalonga, and B. K. Clark, Phys. Rev. Lett 126, 180602 (2021).
- [33] H.-K. Tang, N. Swain, D. C. W. Foo, B. J. J. Khor, F. F. Assaad, S. Adam, and P. Sengupta, arXiv:2106.08587 (2021).
- [34] K. S. Decker, D. M. Kennes, and C. Karrasch, arXiv:2106.12861.
- [35] H. Burau and M. Heyl, Phys. Rev. Lett. 127, 050601 (2021).
- [36] S. W. Kim, G. De Tomasi, and M. Heyl, arXiv:2105.12740.
- [37] W. D. Roeck and J. Z. Imbrie, Phil. Trans. R. Soc. A 375, 20160422 (2017).
- [38] S. Gopalakrishnan and D. A. Huse, Phys. Rev. B 99, 134305 (2019).
- [39] E. V. Doggen, I. V. Gornyi, A. D. Mirlin, and D. G. Polyakov, Phys. Rev. Lett. 125, 155701 (2020).
- [40] A. Chandran, A. Pal, C. R. Laumann, and A. Scardicchio, Phys. Rev. B 94, 144203 (2016).
- [41] F. Pollmann, V. Khemani, J. I. Cirac, and S. L. Sondhi, Phys. Rev. B 94, 041116(R) (2016).
- [42] T. B. Wahl, A. Pal, and S. H. Simon, Phys. Rev. X 7, 021018 (2017).
- [43] T. B. Wahl, Phys. Rev. B 98, 054204 (2018).
- [44] A. Chan and T. B. Wahl, J. Phys.: Cond. Mat. **32**, 305601 (2020).
- [45] J. Li, A. Chan, and T. B. Wahl, Phys. Rev. B 102, 014205 (2020).
- [46] D. J. Luitz, N. Laflorencie, and F. Alet, Phys. Rev. B 91, 081103 (2015).
- [47] M. Serbyn, Z. Papić, and D. A. Abanin, Phys. Rev. Lett.

- **111**, 127201 (2013).
- [48] D. A. Huse, R. Nandkishore, and V. Oganesyan, Phys. Rev. B 90, 174202 (2014).
- [49] A. Chandran, I. H. Kim, G. Vidal, and D. A. Abanin, Phys. Rev. B 91, 085425 (2015).
- [50] V. Ros, M. Mueller, and A. Scardicchio, Nucl. Phys. B 891, 420 (2015).
- [51] S. Inglis and L. Pollet, Phys. Rev. Lett. 117, 120402 (2016).
- [52] L. Rademaker and M. Ortuño, Phys. Rev. Lett. 116, 010404 (2016).
- [53] C. Monthus, J. Stat. Mech. **2016**, 033101 (2016).
- [54] M. Goihl, M. Gluza, C. Krumnow, and J. Eisert, Phys. Rev. B 97, 134202 (2018).
- [55] A. K. Kulshreshtha, A. Pal, T. B. Wahl, and S. H. Simon, Phys. Rev. B 98, 184201 (2018).
- [56] X. Chen, Z.-C. Gu, Z.-X. Liu, and X.-G. Wen, Phys. Rev. B 87, 155114 (2013).
- [57] H. Singh, B. Ware, R. Vasseur, and S. Gopalakrishnan,

- Phys. Rev. B 103, L220201 (2021).
- [58] I.-D. Potirniche, S. Banerjee, and E. Altman, Phys. Rev. B 99, 205149 (2019).
- [59] V. S. Varadarajan, Supersymmetry for mathematicians: an introduction (American Mathematical Society., 2004).
- [60] N. Bultinck, D. J. Williamson, J. Haegeman, and F. Verstraete, Phys. Rev. B 95, 075108 (2017).
- [61] P. Corboz and G. Vidal, Phys. Rev. B 80, 165129 (2009).
- [62] P. Corboz, G. Evenbly, F. Verstraete, and G. Vidal, Phys. Rev. A 81, 010303 (2010).
- [63] Z.-C. Gu, F. Verstraete, and X.-G. Wen, ArXiv e-prints (2010), arXiv:1004.2563 [cond-mat.str-el].
- [64] C. V. Kraus, N. Schuch, F. Verstraete, and J. I. Cirac, Phys. Rev. A 81, 052338 (2010).
- [65] P. Corboz, R. Orús, B. Bauer, and G. Vidal, Phys. Rev. B 81, 165104 (2010).
- [66] A. Paszke, G. Chanan, Z. Lin, S. G. E. ward Yang, L. Antiga, and Z. Devito, 31st Conf. Neural Inf. Process. Syst. (2017).

Supplemental Material Fermionic Quantum Circuits Reproduce Experimental Two-dimensional Many-body Localization Transition Point

In this Supplemental Material we provide additional details about:

- 1. Diagrammatic approach to fermionic tensor networks
- 2. Optimization of the quantum circuit U
 - Overview
 - Analytical evaluation of the local cost function
 - Numerical computation of the local cost function
- 3. Calculation of entanglement entropy
- 4. Calculation of localization lengths

1. Diagrammatic approach to fermionic tensor networks

Here we review the idea of super vector spaces following Refs. [44, 59, 60], and the diagrammatic approach to fermionic tensor networks introduced in Ref. [44] (see related but different approaches in Refs. [61–65]). A super vector space $V = V^0 \oplus V^1$ is a direct sum of the vector spaces V^0 and V^1 containing even and odd parity vectors, respectively. A vector $|a\rangle \in V$ is homogeneous if it belongs either to V^0 or V^1 , and its parity is denoted by $|a| \in \{0,1\}$, 0 for even and 1 for odd. V^* denotes the dual super vector space. The graded tensor product of two homogeneous vectors $|a_1\rangle$ and $|a_2\rangle$ is $|a_1\rangle \otimes_{\mathbf{g}} |a_2\rangle \in V \otimes_{\mathbf{g}} V$, and its parity is $|a_1| + |a_2| \mod 2$. The reordering of vectors within a graded tensor product is the isomorphism $\mathcal{F}: |a_1\rangle \otimes_{\mathbf{g}} |a_2\rangle \to (-1)^{|a_1||a_2|} |a_2\rangle \otimes_{\mathbf{g}} |a_1\rangle$. The reordering of graded tensor products in $V^* \otimes_{\mathbf{g}} W$, $V \otimes_{\mathbf{g}} W^*$ and $V^* \otimes_{\mathbf{g}} W^*$ is similarly defined. The contraction \mathcal{C} is the homomorphism $\mathcal{C}: \langle a_1|\otimes_{\mathbf{g}} |a_2\rangle \to \langle a_1|a_2\rangle$. An operator acting on the super vector space V is $\hat{O} = \sum_{a,b} O_{a,b} |a\rangle \otimes_{\mathbf{g}} \langle b| \in V \otimes_{\mathbf{g}} V^*$, which has parity $|O| := |a| + |b| \mod 2$ (where $|a\rangle$ and $|b\rangle$ denote basis vectors with a fixed parity). Higher rank operators are similarly defined.

Our diagrammatic representation of the fermionic tensor network approach is as follows:

- 1. Fermionic ordering of \mathbb{Z}_2 graded tensor products is represented by a single directed line in red passing through all elements of the super vector space (represented as open black legs in Fig. S1).
- 2. Kets (Bras) of the (dual) super vector space $V = V^0 \oplus V^1$ (V^*) are represented as open legs in black that point along (against) the direction of the arrow.

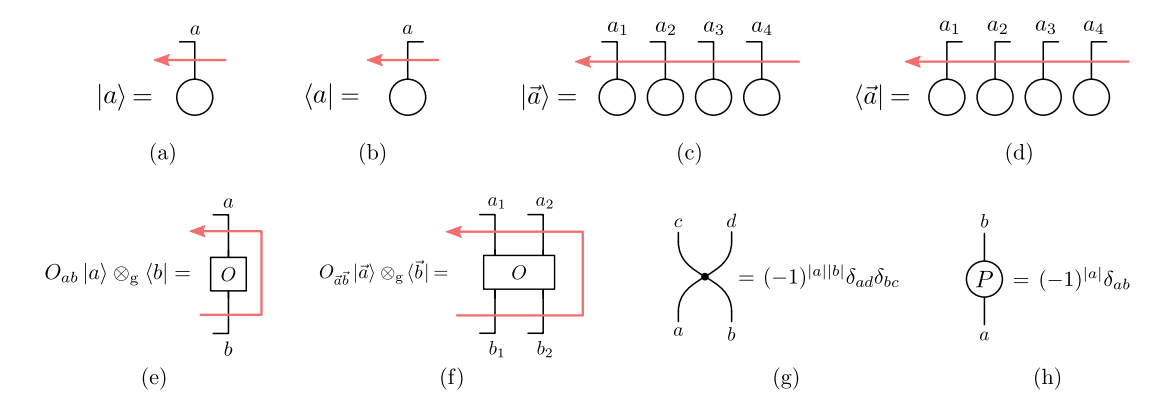


FIG. S1. Diagrammatic representation of (a) a ket $|a\rangle$; (b) a bra $\langle a|$; (c) a many-body ket $|\vec{a}\rangle$; (d) a bra $\langle \vec{a}|$ in the standard ordering; (e) a rank-2 operator \hat{O} ; (f) a many-body operator \hat{O} in the standard form; (g) the fermionic swap gate; and (h) the parity gate.

3. Fermionic reordering of $|a_1\rangle$ and $|a_2\rangle$ gives rise to a parity-dependent sign $(-1)^{|a_1||a_2|}$ which is represented as a crossing between two open legs, denoted as a black dot.

An example is the supertrace of a rank-2 operator \hat{O} , which is written algebraically as

$$\operatorname{sTr}(\hat{O}) := \mathcal{C}\left(\sum_{a,b} O_{ab} |a\rangle \otimes_{\operatorname{g}} \langle b|\right) = \mathcal{C}\left(\sum_{a,b} O_{ab} (-1)^{|a||b|} \langle b| \otimes_{\operatorname{g}} |a\rangle\right) = \sum_{a} (-1)^{|a|} O_{aa} = \operatorname{tr}(PO).$$

Diagrammatically, we have

where $P_{ij} = (-1)^{|i|} \delta_{ij}$ is the parity operator (see Fig. S1). Due to the additional parity operator appearing in the supertrace, the conventional fermionic trace operation of a rank-2 operator in the standard form is implemented as follows,

$$\operatorname{Tr}(\hat{O}) := \mathcal{C}\left(\sum_{a,b,c} (-1)^{|c|} |c\rangle \otimes_{\mathbf{g}} \langle c| \otimes_{\mathbf{g}} O_{ab} |a\rangle \otimes \langle b|\right) = \operatorname{tr}(O) . \tag{S1}$$

Lastly, we show two identities concerning the fermionic swap gates in Fig. S2.

FIG. S2. (a) Fermionic swap gates acting on one leg of tensor \hat{O} can be exchanged with swap gates acting on the complementary set of legs of \hat{O} if \hat{O} is even. If \hat{O} is odd, an additional parity gate appears. (b) A line that crosses all legs of an operator \hat{O} can be simplified according to the parity of the operator \hat{O} .

2. Optimization of the quantum circuit \tilde{U}

Overview

In order to find approximate LIOMs which commute with the Hamiltonian H as well as possible, we minimize the cost function [27, 42]

$$f(\tilde{U}) = \frac{1}{2N^2 4^{N^2}} \sum_{i} \sum_{\mu=\uparrow,\downarrow} \operatorname{Tr}([H, \tilde{\tau}_{i,\mu}^z]^{\dagger} [H, \tilde{\tau}_{i,\mu}^z])$$

$$= \frac{1}{N^2 4^{N^2}} \sum_{i} \sum_{\mu=\uparrow,\downarrow} \left[\operatorname{Tr}(H^2(\tilde{\tau}_{\mu,i}^z)^2) - \operatorname{Tr}(H\tilde{\tau}_{i,\mu}^z H\tilde{\tau}_{i,\mu}^z) \right]. \tag{S2}$$

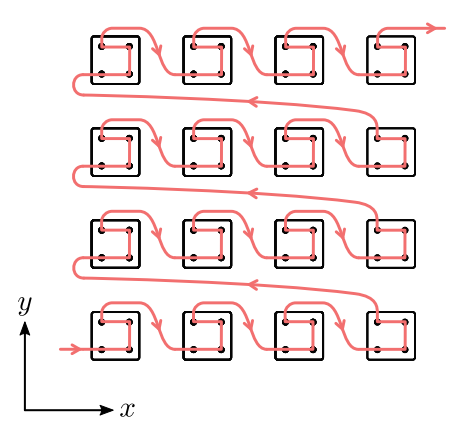


FIG. S3. Chosen ordering of the fermionic operators. Each square contains four sites on which a red gate in Fig. 1 acts.

The sums over sites i and spin μ produce $2N^2$ terms, and the dimension of the overall Fock space is 4^{N^2} , so the factor of $1/(2N^24^{N^2})$ has been included to ensure that $f(\tilde{U})$ becomes an $\mathcal{O}(1)$ number. The first term in the bracket of Eq. (S2) reduces to the constant $\mathrm{Tr}(H^2)$, since $(\tilde{\tau}^z_{i,\mu})^2 = (\sigma^z_{i,\mu})^2 = \mathbb{1}$. The cost function then effectively reduces to a sum of $-\mathrm{Tr}(H\tilde{\tau}^z_{i,\mu}H\tilde{\tau}^z_{i,\mu})$ terms, each of which can be calculated via a local tensor network contraction as explained in the following section.

The optimization is possible for large values of N since the computation time scales linearly with the system size due to the quantum circuit \tilde{U} being built up of smaller unitaries acting on patches of 2×2 sites, cf. Fig 1. Those unitaries are taken to be real and particle number preserving, as the same applies to the Hamiltonian. (This is expected not to reduce the accuracy of the approximation significantly [27, 42].) The small unitaries are thus orthogonal block-diagonal matrices whose diagonal blocks can be parameterized as $u_{\text{block}} = e^A$, where the real anti-symmetric matrix $A = -A^{\top}$ contains the (real) parameters to be optimized.

For the Hamiltonian in Eq. (1), we have f(1) = 4J, regardless of the values of V and Δ . We choose to initialize all unitaries (and consequently \tilde{U}) as identities and set J=1. Thus the cost function takes the initial value of f=4. After performing the optimization, we observe the cost function converging to $f\approx 2$ for small disorder strength ($\Delta \approx 1$), and to as small as $f\approx 0.1$ for large disorder strength ($\Delta > 20$).

Due to virtual memory constraints, we run the optimization by sweeping across the system and optimizing one small unitary at a time. We verified (using a spinless fermionic model) that the sweeping method results in no loss of accuracy compared to simultaneous updating of all parameters. The optimization was performed with the l-BFGS algorithm with automatic differentiation using the PyTorch library [66].

Analytical evaluation of the local cost function

In this section, we show how to compute the cost function contribution, $-\operatorname{Tr}(H\tilde{\tau}^z_{i,\mu}H\tilde{\tau}^z_{i,\mu})$, by evaluating the fermionic contractions within the fermionic trace operation. For the representation of the fermionic operators as matrices, we choose the fermionic ordering shown in Fig. S3. The operator $\tilde{\tau}^z_{i,\mu} = \tilde{U}\sigma^z_{i,\mu}\tilde{U}^{\dagger}$ is a contraction of fermionic operators, and is nontrivial only over a 4×4 region due to its causal cone structure, which arises from the fact that all unitaries in \tilde{U} and their conjugates in \tilde{U}^{\dagger} cancel out (even in the presence of fermionic swap gates), except a local set of unitaries, as illustrated in Fig. S4. When calculating $-\operatorname{Tr}(H\tilde{\tau}^z_{i,\mu}H\tilde{\tau}^z_{i,\mu})$, we consider H as a sum of local terms, and note that those terms that lie entirely outside the 4×4 causal cone region give a constant contribution to the cost function, and can therefore be ignored. By only including the Hamiltonian terms inside the causal cone, $-\operatorname{tr}(H\tilde{\tau}^z_{i,\mu}H\tilde{\tau}^z_{i,\mu})$ becomes a sum of local tensor network contractions.

Specifically, we write the Hamiltonian $H = \sum_k h_k$ as a sum of 2-site operators over all pairs of nearest neighbors. The local action of the 2-site operators h_k is given by [ignoring Jordan-Wigner (JW) strings of fermion parity

¹ To clarify the relation between h_k^{loc} and h_k : h_k^{loc} is a 2-site operator, i.e. a 16×16 matrix. $h_k \equiv \mathbb{1} \otimes \ldots \otimes \mathbb{1} \otimes h_k^{\text{loc}} \otimes \mathbb{1} \otimes \ldots \otimes \mathbb{1}$ is an operator that acts *non-trivially* on two sites but is formally a $4^{N^2} \times 4^{N^2}$ matrix.

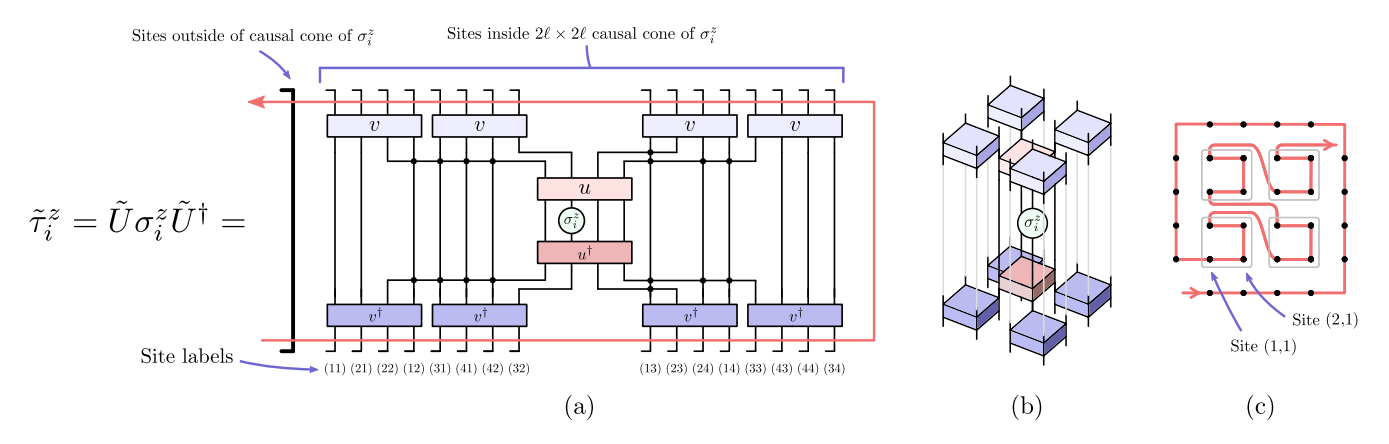


FIG. S4. (a) Diagrammatic representation of $\tilde{\tau}_{i,\mu}^z = \tilde{U}\sigma_{i,\mu}^z \tilde{U}^\dagger$ as a 2D diagram. For simplicity, the index μ is suppressed in the diagrams. The sites inside the causal cone of $\sigma_{i,\mu}^z$ are illustrated explicitly, with the fermionic ordering specified in (c), while the ones outside are represented as a thick line. (b) $\tilde{\tau}_{i,\mu}^z = \tilde{U}\sigma_{i,\mu}^z \tilde{U}^\dagger$ as a 3D diagram, where we have omitted the sites outside the causal cone of $\sigma_{i,\mu}^z$ and the swap gates (explicitly shown in (a)) for simplicity. (c) New fermionic ordering for the 32 sites inside of and surrounding the causal cone of $\sigma_{i,\mu}^z$. The ordering of other sites in the system can be arbitrarily arranged once the gates in \tilde{U} outside the causal cone of $\sigma_{i,\mu}^z$ have been canceled, as the identity lines can be dragged through the even operator $\tilde{\tau}_{i,z}^\mu$.

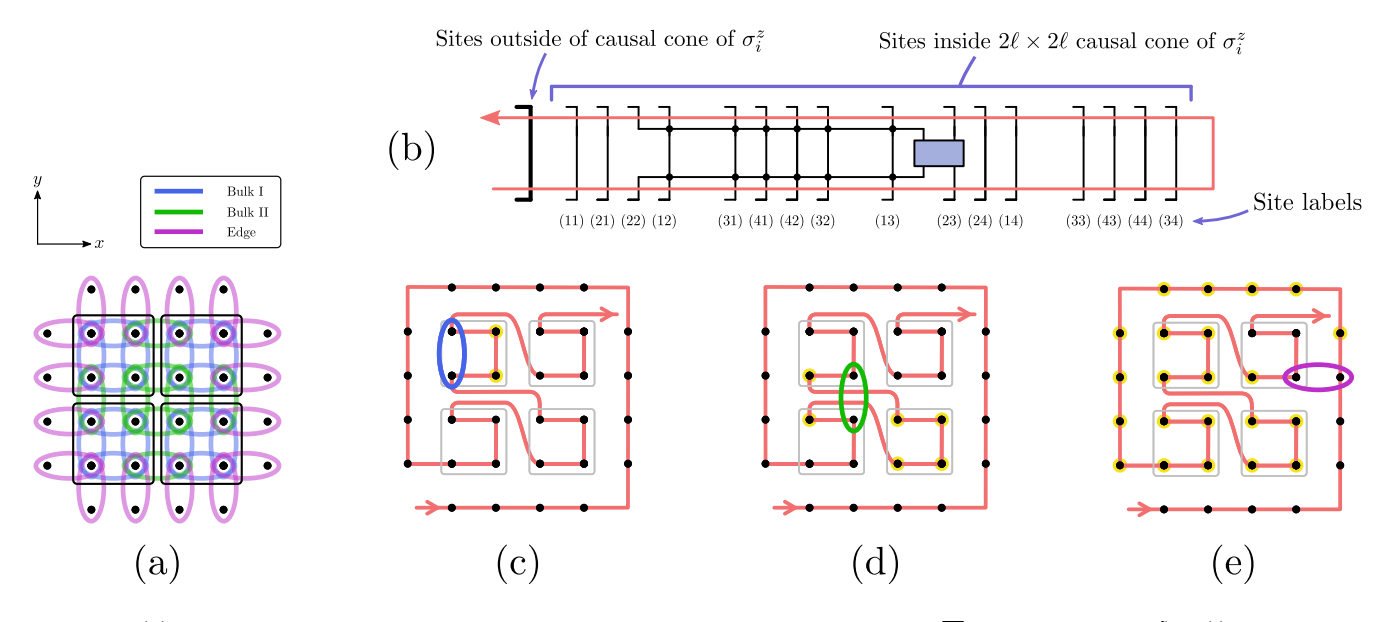


FIG. S5. (a) Classification of three types of contributions to the Hamiltonian $H = \sum_k h_k$ for a given $\sigma^z_{i,\mu}$: (i) Bulk-I terms (blue), which reside within 2×2 plaquettes (black squares); (ii) bulk-II terms (green) which act across two plaquettes; and (iii) edge terms (purple) which straddle across the boundary of the causal cone. (b) As an example, we illustrate the fermionic tensor network of a bulk-II type h_k that acts on site (2,2) and (2,3). The coordinates within the causal cone are defined according to Fig. S4c. The location of this term is illustrated in (d). (c) A bulk-I type h_k (blue) can give rise to JW string (yellow) within a plaquette. (d) A bulk-II type h_k (green) can give rise to JW string (yellow) in multiple plaquettes. The fermionic tensor network of this term is illustrated in (b). (e) An edge type h_k (purple) can give rise to JW string (yellow) in multiple plaquettes and at sites surrounding the causal cone.

operators on other sites; see next paragraph]

$$h_k^{\text{loc}} = -J\left((c_{\uparrow}^{\dagger}Z) \otimes c_{\uparrow} + (c_{\downarrow}^{\dagger}Z) \otimes c_{\downarrow} + (Zc_{\uparrow}) \otimes c_{\uparrow}^{\dagger} + (Zc_{\downarrow}) \otimes c_{\downarrow}^{\dagger}\right) + \frac{1}{2}\left[Vn_{\uparrow}n_{\downarrow} + W(x,y)(n_{\uparrow} + n_{\downarrow})\right] \otimes \mathbb{1} , \qquad (S3)$$

where Z = diag(1, -1, -1, 1) is the local parity operator, and c_{μ}^{\dagger} and c_{μ} are creation and annihilation operators acting on a single site (i.e. 4×4 matrices). $n_{\mu} = c_{\mu}^{\dagger} c_{\mu}$ and $W(x, y) = \Delta[\cos(2\pi(\beta_x x + \delta x)) + \cos(2\pi(\beta_y y + \delta y))]$, where (x, y) is the coordinate of one of the two sites that h_k acts on (we will use the convention that it is always the coordinate

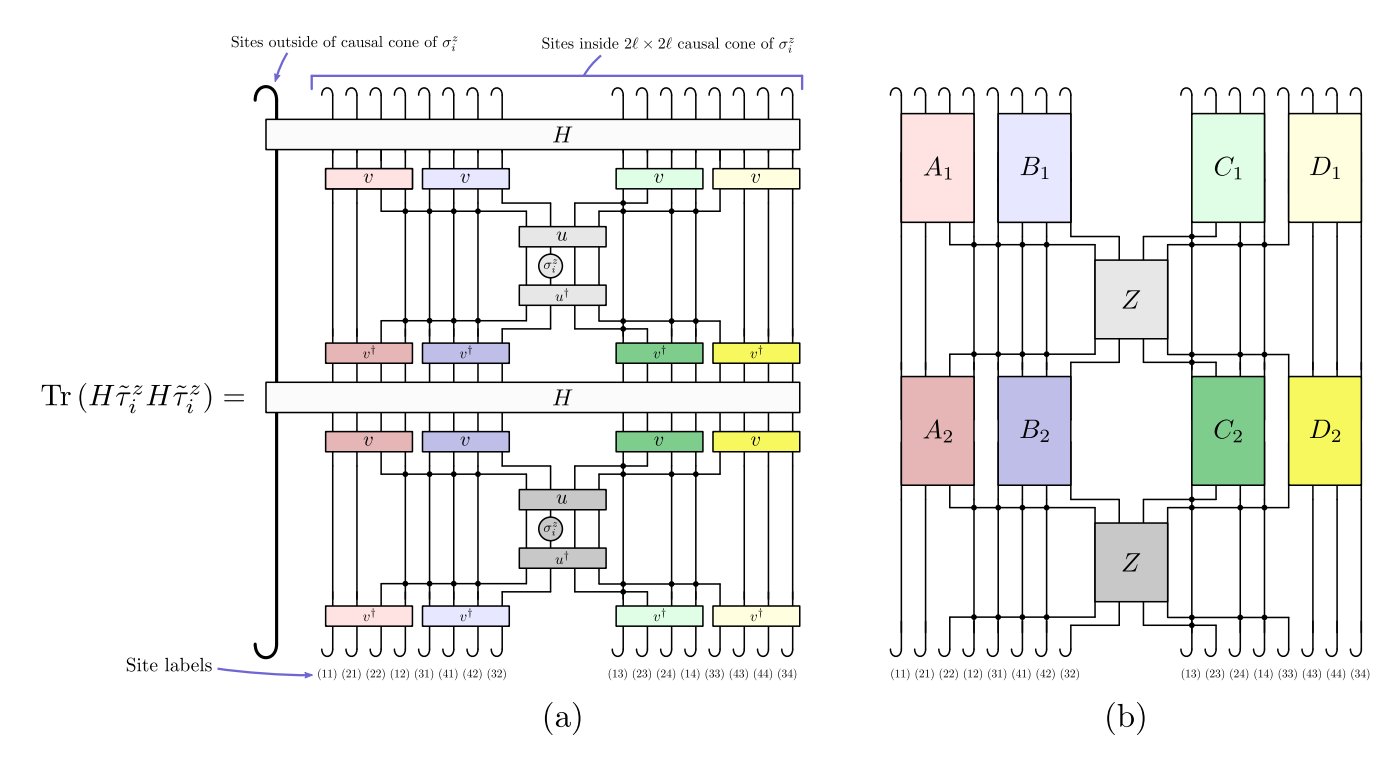


FIG. S6. (a) Diagrammatic representation of the local contributions to the cost function. Additional subscripts of u, v, σ_i^z and $\tilde{\tau}_i^z$ have been suppressed for simplicity. By expanding the Hamiltonian $H = \sum_k h_k$ in terms of local contributions (see Figs. S5 and S7), we can rewrite the cost function in (a) as a sum of tensor network contractions of the form in (b). The tensors with the same color in (a) are grouped into one tensor with the same color in (b) (after the decomposition of H).

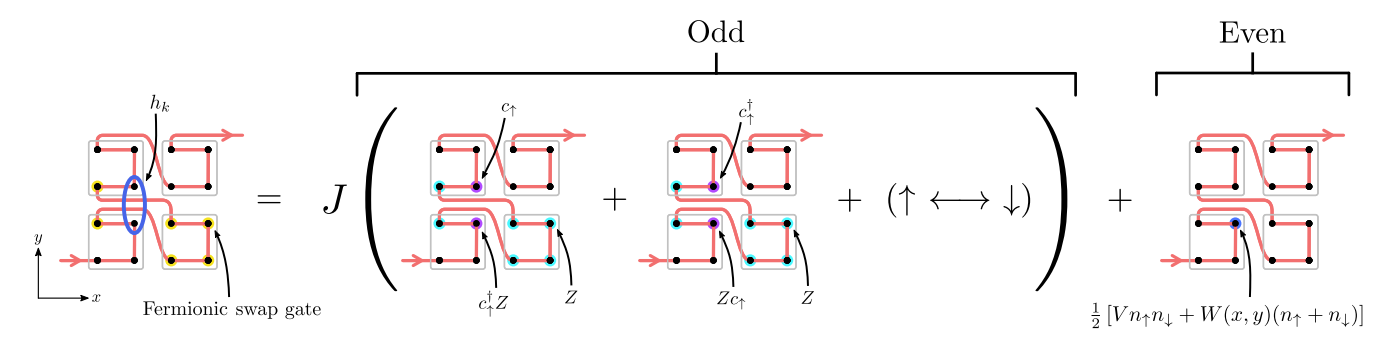


FIG. S7. A graphical depiction of Eq. (S3), for an example of a Bulk-II type h_k operator. On the left, we illustrate h_k in the notation of Fig. S5 (sites outside of the 4×4 causal cone are not shown). On the right, we illustrate a sum of five tensor products.

of the left or lower site, when h_k lies horizontally or vertically, respectively). We thus have $-\operatorname{Tr}(H\tilde{\tau}_{i,\mu}^zH\tilde{\tau}_{i,\mu}^z) = -\sum_{k,l}\operatorname{Tr}(h_k\tilde{\tau}_{i,\mu}^zh_l\tilde{\tau}_{i,\mu}^z)$. Now we partition the 4×4 causal cone region (where $\tilde{\tau}_{i,\mu}^z$ is non-trivially supported) into four 2×2 plaquettes as in the black squares in Fig. S5a. The h_k 's that act non-trivially on the 4×4 causal cone region can be classified as (Fig. S5a): (i) Bulk-I terms, which reside within one of the plaquettes; (ii) bulk-II terms, which act across two plaquettes; and (iii) edge terms, which straddle across the boundary of the causal cone of $\tilde{\tau}_{i,\mu}^z$. If both h_k and h_l are bulk-I terms, i.e. they lie within plaquettes, $h_k\tilde{\tau}_{i,\mu}^zh_l\tilde{\tau}_{i,\mu}^z$ reduces to an expression of the form of Fig. S6b, which is relatively easy to contract (see the description of the contraction algorithm below). If either h_k or h_l is a bulk-II or edge term, i.e. $h_{k/l}$ lies across plaquettes or the edge, then h_k or h_l is decomposed using Eq. (S3) into a sum of products of on-site operators, so we end up expressing $h_k\tilde{\tau}_{i,\mu}^zh_l\tilde{\tau}_{i,\mu}^z$ as a sum of multiple expressions of the form Fig. S6b.

As mentioned above, it is not strictly true that the 2-site operators h_k can be locally written as in Eq. (S3), due to the presence of JW strings. Specifically, if the 2-site operator h_k lies along the fermionic ordering in Fig. S4c, then the previous paragraphs apply directly. However, if h_k does not lie along the fermionic ordering, then the fermionic

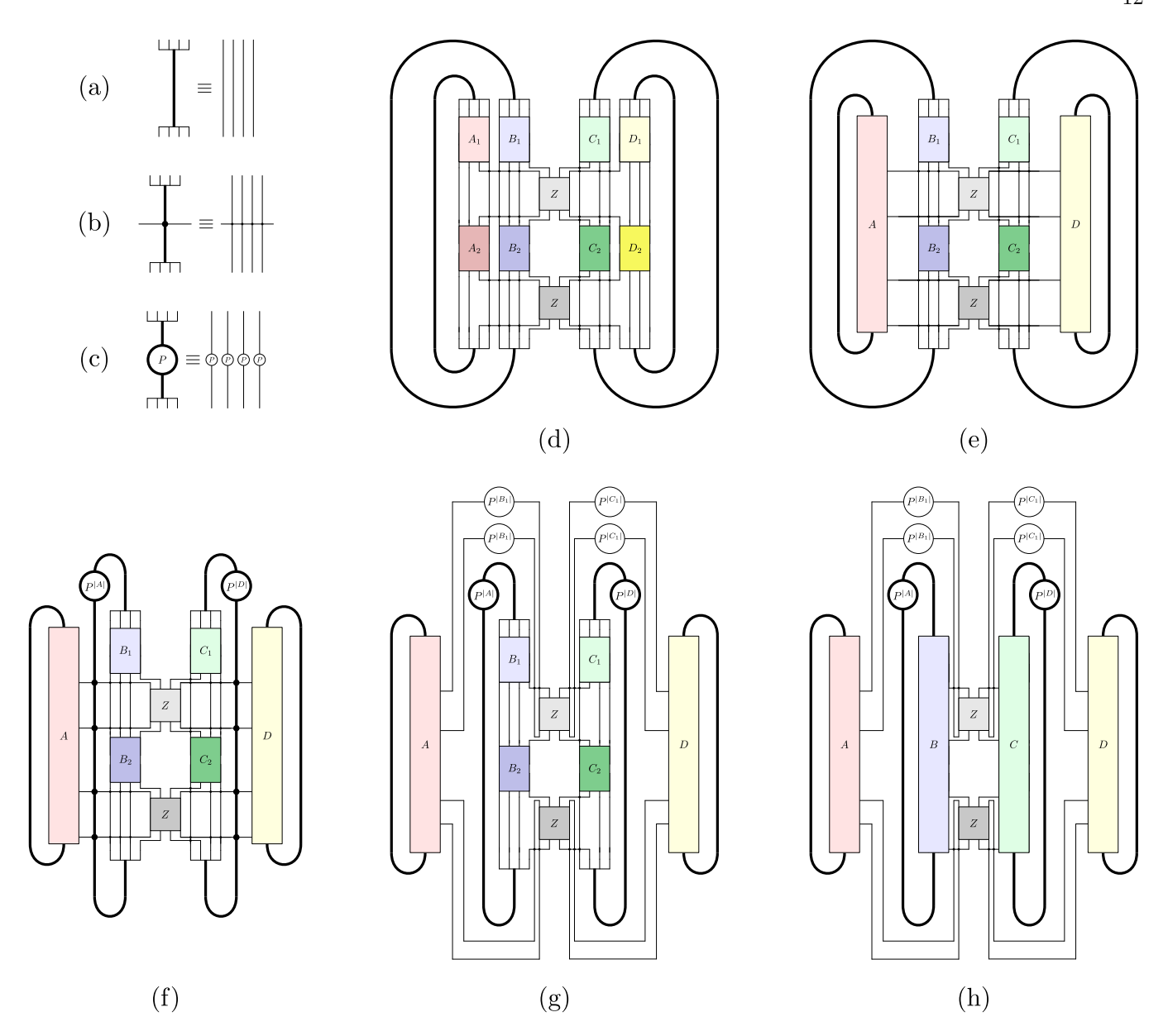


FIG. S8. (a) Definition of a thick line, which represents a collection of four parallel thin lines. (b) A fermionic swap gate or (c) a parity gate acting on a thick line represents fermionic swap gates or parity gates applied separately on the four parallel thin lines. (d) A diagrammatic representation of contributions to the cost function after the evaluation of the fermionic contraction (equivalent to Fig. S6). (e) Definition of tensor A(D) as a combination of the A_1 and A_2 tensors in red (D_1 and D_2 in yellow). (f) Dragging the outermost thick lines in (e) towards the center of the diagram, which gives rise to fermionic swap gates and parity operators according to the identities in Fig. S2. (g) Dragging the four thin lines connected to tensor A (and D) to the top and the bottom of the diagram. Again, fermionic swap gates and parity operators appear according to the identities in Fig. S2. (h) The final simplified diagram is obtained by defining tensor B(C) as a combination of the B_1 and B_2 tensors in blue (C_1 and C_2 in green).

contractions give rise to a series of fermionic swap gates, which we call a JW string, located along the fermionic ordering and in between the creation and annihilation operators of h_k . As an example, we consider a bulk-II term h_k illustrated in Fig. S5d, which can be expressed in the tensor network notation as Fig. S5b. This decomposition and resulting JW strings are shown in Fig. S7. Generally, a JW string appears for bulk-I term h_k if h_k acts within a plaquette on the bottom left and top left site, and for all bulk-II and edge terms.

In the paragraphs above, we have evaluated the fermionic contraction in the local cost function $-\operatorname{Tr}(H\tilde{\tau}^z_{i,\mu}H\tilde{\tau}^z_{i,\mu})$. We showed that the cost function involves calculating $h_k\tilde{\tau}^z_{i,\mu}h_l\tilde{\tau}^z_{i,\mu}$ terms and summing over all the h_k and h_l operators that intersect the 4×4 causal cone of $\sigma^z_{i,\mu}$. By decomposing $h_k\tilde{\tau}^z_{i,\mu}h_l\tilde{\tau}^z_{i,\mu}$ whenever necessary, we can write the local

cost function in the form depicted in Fig. S6b: We further simplify Fig. S6a using tensor network techniques. For a given h_k and h_l , we combine pairs of unitaries (u^{\dagger}, u) and (v^{\dagger}, v) with the intervening Hamiltonian terms in Fig. S6a to obtain the diagram in Fig. S6b.

Next, we simplify Fig. S6b in Fig. S8 by contracting together tensors and dragging lines across tensors using the identities described in Fig. S2. In Fig. S8, we adopt the convention of thick lines which represent four parallel thin lines as described in Fig. S8a-c. We use the intermediate steps shown in Fig. S8d-g to arrive at the final simplified diagram in Fig. S8h.

In short, the cost function $-\operatorname{Tr}(H\tilde{\tau}_{i,\mu}^zH\tilde{\tau}_{i,\mu}^z)$ can be evaluated as Fig. S6a. After expanding the Hamiltonian in terms of local contributions given in Fig. S5 using the expansion in Fig. S7, the fermionic contractions within the trace can be performed, and the cost function can be expressed as a sum of tensor networks of the form shown in Fig. S8h.

Numerical computation of the local cost function

In practice, it is not the most efficient way to loop over h_k and h_l . Some speedup can be achieved by organizing the sums in specific ways. Additionally, some subtleties arise when h_k and h_l lie on the edge of the causal cone region. In this section, we discuss the algorithm used to numerically calculate the local cost function as a sum over tensor networks of the type shown in Fig. S8h.

First, we make a parenthetical comment about the dimensionality of operators. In the below, we will refer to operators that act only on a local region. In the interest of making the equations consistent in the simplest way possible, let us adopt the convention that operators are defined on the full Fock space. So for example, h_k acts non-trivially on 2 sites in the 4^{N^2} -dimensional Fock space.

Our aim is to compute $\text{Tr}(H\tilde{\tau}_{i,\mu}^z H\tilde{\tau}_{i,\mu}^z)$. Recall that only Hamiltonian terms that have non-trivial support in the $\tilde{\tau}_{i,\mu}^z$ causal cone need to be considered. For a given causal cone, we decompose the Hamiltonian as $H = \sum_{k \in \text{ outside }} h_k + \sum_{k \in \text{ causal cone}} h_k \equiv H_{\bar{c}} + H_c$. Within the sum over terms in the causal cone, h_k terms may lie within a plaquette (Bulk I), across two plaquettes but still in the bulk (Bulk II), or on the edge, as depicted in Fig. S5. Let us write

$$H_{c} = \sum_{\substack{k \in \text{Bulk II}}} h_{k} + \sum_{\substack{k \in \text{Bulk III}}} h_{k} + \sum_{\substack{k \in \text{Edge}}} h_{k} . \tag{S4}$$

Furthermore, we define

$$H_{\square} \equiv \sum_{\substack{k \in \text{Bulk I}}} h_k + \sum_{\substack{k \in \text{Edge}}} h'_k , \qquad (S5)$$

where h'_k is the operator acting on the edge with the outside leg traced out,

$$\frac{h'_k}{h'_k} \equiv \frac{h_k}{h_k} \tag{S6}$$

where both operators have to be thought of as tensor products with 1 on all other sites. In other words, H_{\Box} is defined to be H_c but without the Bulk II terms, and with the edge legs traced out (so it is an operator acting non-trivially on only 16 sites instead of 32 sites). We can now write the local cost function in a form that involves much fewer tensor

network contractions,

$$\operatorname{Tr}(H_{c}\tilde{\tau}_{i,\mu}^{z}H_{c}\tilde{\tau}_{i,\mu}^{z}) = \underbrace{\operatorname{Tr}(H_{\Box}\tilde{\tau}_{i,\mu}^{z}H_{\Box}\tilde{\tau}_{i,\mu}^{z})}_{f_{1}} + 2\underbrace{\sum_{\substack{k \in \text{Bulk II} \\ \text{Bulk II}}} \operatorname{Tr}(H_{\Box}\tilde{\tau}_{i,\mu}^{z}h_{k}\tilde{\tau}_{i,\mu}^{z})}_{f_{2}} + \underbrace{\sum_{\substack{k \in \text{Bulk II Bulk II} \\ \text{Bulk II Bulk II}}} \operatorname{Tr}(h_{k}\tilde{\tau}_{i,\mu}^{z}h_{l}\tilde{\tau}_{i,\mu}^{z})}_{f_{3}} + \underbrace{\sum_{\substack{k \in \text{Edge} \\ \text{Edge}}} \left[\operatorname{Tr}(h_{k}\tilde{\tau}_{i,\mu}^{z}h_{k}\tilde{\tau}_{i,\mu}^{z}) - \operatorname{Tr}(h_{k}'\tilde{\tau}_{i,\mu}^{z}h_{k}'\tilde{\tau}_{i,\mu}^{z})\right]}_{f_{4}}. \quad (S7)$$

The four parts labeled f_1 , f_2 , f_3 , and f_4 can now be calculated separately, with f_3 being the most computationally expensive term to calculate.

Note that the right hand side of Eq. (S7), with the exception of the first term in f_4 , only contains operators that act non-trivially within the 4×4 region. Thus we can take the trace with the above described contraction algorithm, and then normalize by a factor of $1/4^{16}$. (For the first term in f_4 , we need to normalize by $1/4^{17}$, as one of the tensors A, B, C, D obtains one additional leg.) The bulk-II h_k operators as well as the edge h_k operators in the first term of f_4 , need to be decomposed into a sum of tensor products, as in Eq. (S3). As a result, the sum over the bulk-II operators is a sum over 40 terms: 8 bulk-II terms h_k , multiplied by 5 contributions per h_k . Thus, we can see that the calculation of f_2 requires 40 trace calculations, and the calculation of f_3 manifestly requires 1600 trace calculations (note that, for the latter case, the number of terms can be halved due to symmetry).

3. Calculation of entanglement entropy

Here we describe the methods used to calculate the transition point Δ_c from the optimized quantum circuit \tilde{U} . Specifically, we describe the computation of the entanglement entropy and its standard deviation (which gives Figs. 2 and 3) for a certain filling fraction ν .

For each site i we first calculate the on-site entanglement entropies averaged over 1,000 eigenstates. Our main quantity of interest is the standard deviation of this average entropy with respect to disorder realizations averaged over sites i [27],

$$\sigma_S(\Delta) = \frac{1}{N^2} \sum_{i} \sigma_{S,i}(\Delta) , \qquad (S8)$$

where N is the linear system size, and $\sigma_{S,i}(\Delta)$ is the standard deviation of the on-site entropies at site i,

$$\sigma_{S,i}(\Delta) = \sqrt{\langle S_i^2(\Delta) \rangle - \langle S_i(\Delta) \rangle^2} \ . \tag{S9}$$

Here $\langle \cdot \rangle$ means an average over all disorder realizations at disorder strength Δ (we used 10 disorder realizations at each Δ), and $S_i(\Delta)$ is the on-site entanglement entropy at site i averaged over $N_{\text{states}} = 1,000$ approximate eigenstates k,

$$S_i(\Delta) = -\frac{1}{N_{\text{states}}} \sum_{k=1}^{N_{\text{states}}} \operatorname{tr}(\rho_i(k) \ln \rho_i(k)) . \tag{S10}$$

The density matrix $\rho_i(k)$ is given by

$$\rho_i(k) = \text{Tr}_{\bar{i}}[|\psi(k)\rangle\langle\psi(k)|] , \qquad (S11)$$

where the partial trace is taken over all sites other than i, and $|\psi(k)\rangle$ is a randomly chosen approximate eigenstate from \tilde{U} obtained by fixing the indices corresponding to the lower legs of Fig. 1a. The graphical representation of this equation is depicted in Fig. S9. Due to the quantum circuit structure, the calculation of $\rho_i(k)$ becomes local.

We can also calculate $\sigma_S(\Delta, \nu)$, the standard deviation of the entropy at some given filling fraction ν . Recall that all (approximate) eigenstates have well-defined particle number, as \tilde{U} is particle-number conserving. The procedure is exactly as described above for calculating $\sigma_S(\Delta)$, except we constrain the random states $|\psi(k)\rangle$ to be of filling

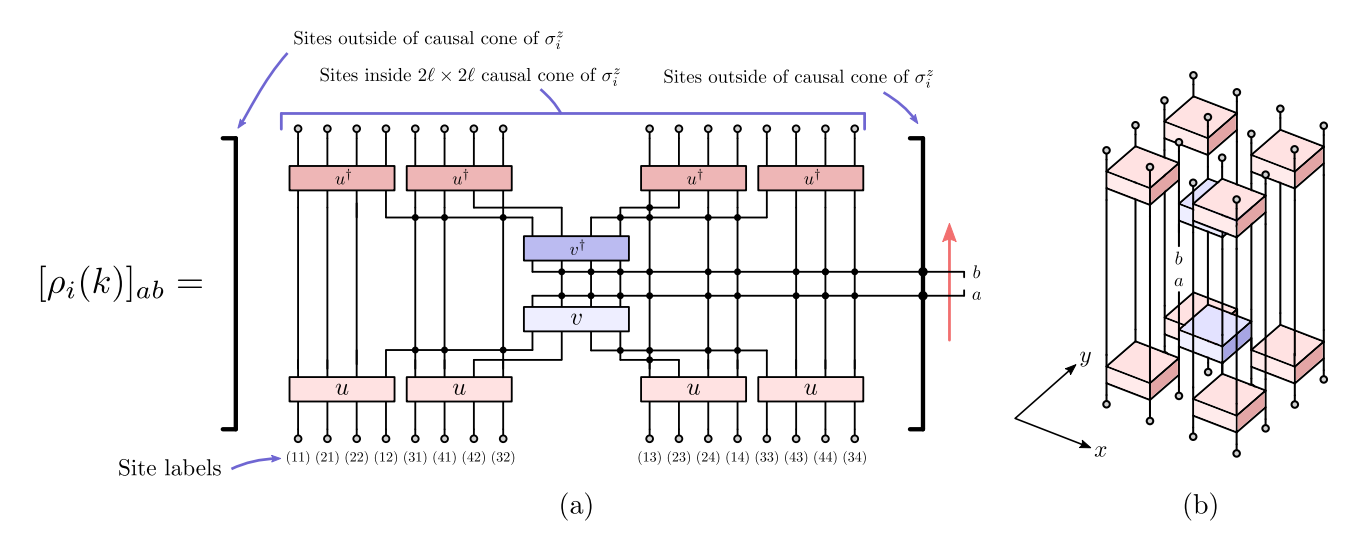


FIG. S9. (a) Diagrammatic representation of $[\rho_i(k)]_{ab} = \text{Tr}_{\bar{i}}[|\psi(k)\rangle\langle\psi(k)|]_{ab}$ as a 2D diagram. The sites inside the causal cone of site i are illustrated explicitly, while the ones outside are represented as a thick lines. (b) $[\rho_i(k)]_{ab} = \text{Tr}_{\bar{i}}[|\psi(k)\rangle\langle\psi(k)|]_{ab}$ as a 3D diagram, where we have omitted the sites outside the causal cone of $\sigma_{i,\mu}^z$ and the swap gates (explicitly shown in (a)) for simplicity. Note that due to the even parity of the unitaries, $[\rho_i(k)]_{ab}$ is non-vanishing only for $|a| + |b| \mod 2 = 0$.

fraction ν by choosing the eigenstates k such that they correspond to an l-bit configuration with overall particle number νN^2 . Also, when calculating the filling fraction dependent entropy $S_i(\Delta, \nu)$, we average over 10,000 instead of 1,000 eigenstates, due to the increased sensitivity to fluctuations in this case.

To obtain the ν -dependent phase diagram as shown in Fig. 3, we compute $\sigma_S(\Delta, \nu)$ for the 21 filling fractions $\nu \in [0.5, 1.5]$ in steps of 0.05. That is, we performed the procedure described above, at each stage constraining the random states $|\psi(k)\rangle$ to have particle numbers $N^2\nu \in [50, 150]$ in steps of 5. These plots, with a third-order polynomial fit, are shown in the inset of Fig. 3 (Note that all 21 curves are on the plot, but to reduce clutter, not all are labeled in the legend). We located the maxima of these curves to find the filling fraction-resolved transition points $\Delta_c(\nu)$, which we plot (together with a fitted fourth order polynomial) to form the filling fraction-dependent phase diagram in the main panel of Fig. 3.

4. Calculation of localization lengths

In this section we discuss the numerically efficient calculation of the localization lengths using Eq. (3). Assuming the operator \mathcal{O} is localized on some site j, we would expect $w_i(\mathcal{O})$ to to scale as $\exp(-\operatorname{dist}(i,j)/\xi_L)$, where ξ_L is the localization length. Given an optimized \tilde{U} , we can use the weight functions of the l-bit operators to discern the average localization length of the system. As we have two l-bit operators per site, we define the weight $w_{ij} \equiv w_i(\tilde{\tau}^z_{j,\uparrow}) + w_i(\tilde{\tau}^z_{j,\downarrow})$. For the weight function of the l-bit operators, we have

$$w_{i}(\tilde{\tau}_{j,\mu}^{z}) = \sum_{\beta,\gamma}' \operatorname{Tr} \left[\left(\tilde{\tau}_{j,\mu}^{z} - \hat{\sigma}_{i,\uparrow}^{\beta} \hat{\sigma}_{i,\downarrow}^{\gamma} \tilde{\tau}_{j,\mu}^{z} \hat{\sigma}_{i,\downarrow}^{\gamma} \hat{\sigma}_{i,\uparrow}^{\beta} \right)^{2} \right] = 2 \sum_{\beta,\gamma}' \operatorname{Tr} \left[\mathbb{1} - \tilde{\tau}_{j,\mu}^{z} \hat{\sigma}_{i,\uparrow}^{\beta} \hat{\sigma}_{i,\downarrow}^{\gamma} \tilde{\tau}_{j,\mu}^{z} \hat{\sigma}_{i,\downarrow}^{\gamma} \hat{\sigma}_{i,\uparrow}^{\beta} \right], \tag{S12}$$

where Tr $(\tilde{\tau}_{j,\mu}^z\hat{\sigma}_{i,\uparrow}^{\beta}\hat{\sigma}_{i,\downarrow}^{\gamma}\tilde{\tau}_{j,\mu}^z\hat{\sigma}_{i,\downarrow}^{\gamma}\hat{\sigma}_{i,\uparrow}^{\beta})$ can be calculated efficiently by the same methods used to calculate Tr $(\tilde{\tau}_{j,\mu}^zh_k\tilde{\tau}_{j,\mu}^zh_l)$ for the cost function. As explained in the main text, the sum \sum' is a sum over all possible $\beta, \gamma \in \{0, x, y, z\}$ except $\beta = \gamma = 0$, i.e. there are 15 terms in this sum.

Note that w_{ij} will be zero if the site i does not lie in the causal cone of $\tilde{\tau}^z_{j,\mu}$. Thus for l-bit operators on a given site j, we can calculate w_{ij} for the sixteen sites i that lie in the causal cone. Due to the geometry, the distance between sites i and j will be either $0, 1, \sqrt{2}, 2, \sqrt{5}$, or $2\sqrt{2}$. For a given site j and the 16 sites i, we plot w_{ij} as a function of $\mathrm{dist}(i,j)$ and fit the data to an exponential curve $Ae^{-\mathrm{dist}(i,j)/\xi_{L,j}}$ to find the localization length $\xi_{L,j}$. We first average the fitted $\xi_{L,j}$ over all sites j, and then average over all disorder realizations at a given Δ , to obtain $\xi_L(\Delta)$.